

THE EFFECT OF SOLUTION TEMPERATURE ON MICROSTRUCTURE EVOLUTION AND MECHANICAL PROPERTIES OF A LOW-SILICON CAST ALUMINUM ALLOY CONTAINING Mn

Dongling Qian, Kai Lan and Yitao Yang 

School of Materials Science and Engineering, Shanghai University, Shanghai 200444, China

Copyright © 2023 American Foundry Society
<https://doi.org/10.1007/s40962-023-01138-y>

Abstract

The detailed investigation of the microstructure evolution in the Al–3.4Si–0.6Mg–0.5Mn alloy, solution-treated at 530, 545, and 560 °C for 4 h, and its corresponding mechanical properties at the T6 heat-treated state, is presented in this study. It was found that the as-cast microstructure of the experimental alloys comprised α -Al, eutectic Si, π -Al₈Mg₃FeSi₆(Mn), and α -Al₁₅(Fe, Mn)₂Si₃ intermetallics. Throughout the solution treatment, the dissolution of blocky π -Fe intermetallics transpired, accompanied by the spheroidization of eutectic Si and precipitation of Mn-enriched dispersoids. As the solution temperature increased, the dissolution of π -Fe intermetallics became more pronounced, leading to their gradual transformation into spherical α -Al₁₅(Fe, Mn)₂Si₃ intermetallics. The alloy subjected to T6 heat treatment, which had been solution-treated at 545 °C for 4 hours,

effectively mitigated the deleterious effects of blocky π -Fe intermetallics and eutectic Si, resulting in a commendable elongation to fracture (7.4%). Furthermore, the precipitation kinetics of Mn-containing dispersoids in the Al–Si–Mg–Mn alloy were markedly influenced by the solution temperature. The elevating solution temperature bolstered the nucleation, growth, and coarsening of dispersoids. The increase in the precipitation of fine dispersoids augmented the resistance to dislocation movement during the strain process, thereby enhancing the yield strength of the alloy.

Keywords: low-silicon cast aluminum alloy, Mn element, solution treatment temperature, Fe-rich intermetallic compounds, dispersion strengthening, mechanical properties

Introduction

Al–Si–Mg alloys are widely employed in the fabrication of automotive parts using permanent mold and low-pressure die casting techniques due to their superior formability.^{1–3} To attain an optimal strength-ductility balance, the T6 heat treatment process is applied to achieve advantageous microstructure preparation in these alloys.^{4,5} However, during the solution treatment, the dissolution of Fe-rich intermetallic compounds (FIMCs), such as β -Al₅FeSi, which are common inclusions detrimental to mechanical properties, presents a considerable challenge.^{6,7}

The incorporation of Mn is a standard practice for modifying Fe-rich phases to enhance the mechanical properties

of Al–Si alloys.^{8,9} However, following the addition of Mn, the formation and modification of FIMCs are not easily controlled during solidification due to non-equilibrium solidification and heterogeneous nucleation among different types of FIMCs.^{10,11} In Al–Si–Mg–Mn alloys, the formation of FIMCs during solidification often deviates from phase diagram predictions. According to previous studies, initial primary or eutectic FIMCs can serve as heterogeneous nucleation sites for subsequent compounds, complicating the formation of FIMCs in the solidification process.¹¹ These FIMCs possess diverse thermal stabilities and negatively affect the alloy's mechanical properties. Consequently, selecting an appropriate solution temperature to ensure optimal dissolution of these FIMCs during solution treatment is of utmost importance.^{4,12} Apart from modifying FIMCs, the introduction of Mn into Al–Si–Mg alloys also triggers the precipitation of Mn-containing dispersoids during solution treatment. This precipitation can obstruct dislocation movement, thereby enhancing

Table 1. Chemical Compositions of A356 and Experimental Alloys (wt%)

	Si	Mg	Fe	Mn	Sr	Ti	Al
A356	7.18	0.37	0.14	–	–	0.16	Balance
Experimental alloy	3.42	0.63	0.18	0.54	0.025	0.06	Balance

Table 2. Heat Treatment Process of Experimental Alloys

	Solution treatment		Aging treatment
Alloy A	530 °C/4 h	Water	180 °C/8h
Alloy B	545 °C/4 h	quench	
Alloy C	560 °C/4 h		

alloy strength.^{13–16} Several studies have reported the precipitation of Mn-containing dispersoids in Al–Si–Mg–Mn and Al–Mg–Si–Mn alloys during solution or homogenization treatment.^{17–20} These dispersoids have a partially coherent interface with the Al matrix, and their size and distribution are contingent on the chosen heating temperature.^{19,21} Nevertheless, the interaction between dispersoids and Fe-rich phases during solution treatment has seldom been reported. Additional experimental evidence is needed to elucidate the transformation of Fe-rich phases and dispersion strengthening effect in Al–Si–Mg–Mn alloys at varying solution temperatures.

Furthermore, solution treatment generates a supersaturated solid solution that sets the stage for subsequent artificial aging. During this process, fine and coherent Mg–Si precipitates are formed, yielding the desired strength for the casting.^{4,22,23} It is imperative to elucidate the correlation between phase transitions and solution temperature, as it governs the dissolution of Mg-containing intermetallic compounds and the supersaturation of Mg concentration in the matrix.^{24–26}

In the case of Al–Si–Mg–Mn alloys, the choice of solution temperature determines the dissolution of coarse FIMCs, the precipitation of dispersoids, and the supersaturated solute concentration (such as Mg) within the matrix. The interplay among these factors, however, remains to be elucidated. Furthermore, a comprehensive consideration of their influence on mechanical properties is necessitated. The objective of this study is to assess the impact of solution temperature on the evolution of microstructure and mechanical properties in Al–Si–Mg–Mn alloys and to propose a viable strategy for optimizing the solution process. The precipitation behavior of dispersoids and the transformation of Fe-rich intermetallics at varying solution temperatures were thoroughly explored. Moreover, the dispersion strengthening effect of Al–Si–Mg–Mn alloys treated at different solution temperatures was scrutinized.

Experimental Procedures

The experimental alloys were formulated in an induction furnace through the melting of commercially pure Al and A356, in addition to master alloys Al–10Mg, Al–10Mn, and Al–10Sr, by weight. Subsequently, these were cast into a permanent mold to create cylindrical ingots, each with a diameter of 50 mm and length of 125 mm. The compositions of the employed A356 and the experimental alloys are presented in Table 1. Post-casting, a T6 heat treatment was performed on the ingots, which involved a solution treatment at different temperatures (530, 545, and 560 °C, ± 1 °C) for 4 h, followed by water quenching. Subsequently, artificial aging was conducted at 180 °C for 8 h using a Nabertherm furnace with an accuracy of ± 1 °C. The Al–Si–Mg–Mn alloys, which were solution-treated at varying temperatures (530, 545, and 560 °C), are henceforth referred to as alloy A, B, and C, respectively, as detailed in Table 2. Tensile test samples, with a gage length of 30 mm and diameter of 6 mm, were cut from the cylindrical bars.

A metallographic sample was procured from a position 15 mm above the bottom of the ingot, following which standard metallographic methods were utilized for sample preparation. This process involved initial grinding with a sequence of grit papers, followed by polishing using 0.5 μm diamond polishing paste. Subsequently, the samples were etched with 0.5 vol% HF acid. Microstructural investigations of the experimental samples were undertaken using an optical microscope (OM, Nikon LV150) and a scanning electron microscope (SEM, SHU-SU1510). A JEM-2100F transmission electron microscope (TEM) was employed to observe the morphology and size distribution of the dispersoids, as well as to obtain their high-resolution image. TEM foils were generated through electrolytic thinning in an electrolyte, composed of 75% methanol and 25% nitric acid, at -28 °C using a voltage of 18 V. The average sizes of eutectic Si, the size distribution of the Mn-containing dispersoids, and the area

fraction of the Fe-rich intermetallics in the different alloys were quantified using Image Pro Plus software. The statistical results were derived from the average value of ten field view measurements, with the particle size measured based on equivalent area diameters. The compositions of the Fe-rich intermetallics and the dispersoids were evaluated via energy-dispersive X-ray spectroscopy (EDS) in the SHU-SU1510 SEM and JEM-2100F TEM. The equilibrium solidification process of the Al-3.4Si-0.6Mg-0.5Mn-0.2Fe alloy was computed utilizing Thermo-Calc software.

Experimental Results

Microstructure of As-Cast Al-Si-Mg-Mn Alloys

Figure 1 illustrates the characteristic microstructures of the as-cast Al-Si-Mg-Mn alloy. In the as-cast alloy, the fibrous eutectic Si and two distinct Fe-rich intermetallic compounds (FIMCs) present in the eutectic area were identified. The Energy-Dispersive Spectroscopy (EDS) results pertaining to the two FIMCs aligned with the previously reported π -Al₈Mg₃FeSi₆(Mn) phases and α -Al₁₅(Fe, Mn)₂Si₃ phases in an atomic ratio as demonstrated in Figure 1b, c. This concordance substantiates the modification of acicular Fe-rich phases (β -Al₅FeSi) existent in Al-Si-Mg alloy devoid of Mn.²⁷ As prior studies suggest, these FIMCs in Al-Si-Mg alloys possess varying compositions and function as solid solution compounds.^{28,29} Transition element Mn is known to incorporate into Fe-rich phases and substitute certain atomic positions²⁹. Table 3 lists the elemental concentrations in the α -Al matrix of the as-cast alloys, displaying average concentrations of Mn, Mg, and Si to be 0.29, 0.26, and 1.31 wt%, respectively. At 20 °C, the equilibrium solubility of Mn in Al is 0.06 wt%.¹⁶ Deep etching of SEM observations from the samples reveal an absence of dispersoids, indicating a supersaturation of Mn in the α -Al matrix.

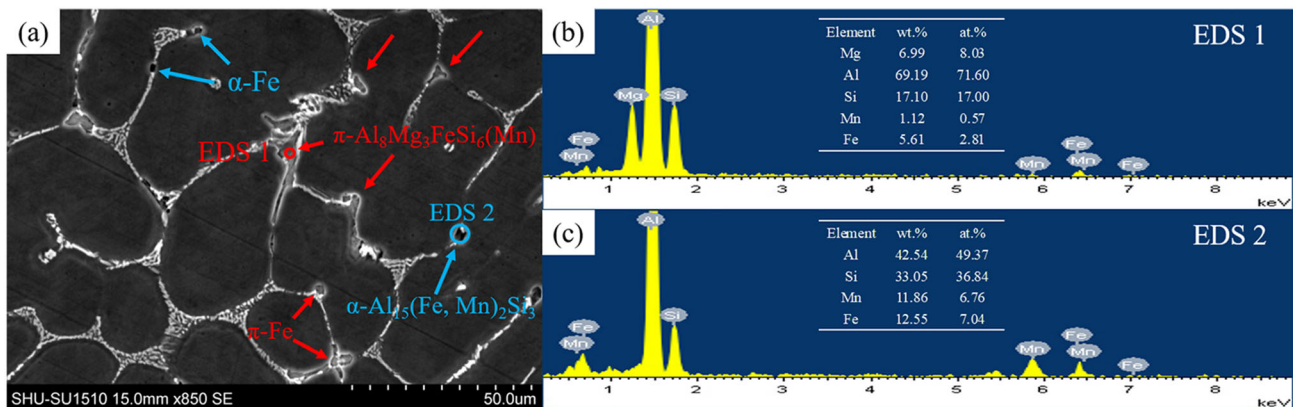


Figure 1. (a) SEM images of the microstructure and (b, c) EDS analysis of the FIMCs in the as-cast Al-Si-Mg-Mn alloy.

The Evolution of Eutectic Si and Rich-Fe Intermetallics with the Different Solution Temperatures

Figure 2 illustrates the microstructure of both the as-cast alloy and T6 heat-treated alloys A, B, and C. Post-T6 heat treatment, a portion of the eutectic Si exhibited an incompletely fragmented block morphology in alloy A (as illustrated in Figure 2b), while in alloys B and C, the fibrous Si particles from the as-cast state had transitioned into a spheroidized form (Figure 2c, d). Table 4 presents the average size of eutectic Si in the three T6 heat-treated alloys, indicating that an elevated solution temperature facilitates the spheroidization of eutectic Si.

Contrasting with the eutectic Si, which demonstrates homogeneously distributed spheroids within the eutectic regions as observed in Figure 2, the Fe-rich intermetallic compounds (FIMCs) predominantly exhibit needles, intermittent granules, and coarser spheroids in the T6 heat-treated alloys A, B, and C, respectively. For elucidating the transformation of FIMCs at varying solution temperatures, the distinct morphology of the FIMCs was unveiled through high magnification SEM images, while their phase compositions were monitored via EDS analysis, as depicted in Figure 3. In alloy A (Figure 3a, b), the FIMCs were identified as π -Al₈FeMg₃Si₆(Mn), revealing an initially dissolved needle, which might trigger stress accumulation and negatively impact the fracture toughness of the alloy.

Table 3. The Mean Concentration (wt%) of Mn, Mg and Si Elements Within the α -Al Matrix of The As-Cast Al-Si-Mg-Mn Alloy

Alloy	Mn	Mg	Si
As-cast	0.29±0.03	0.26±0.02	1.31±0.03

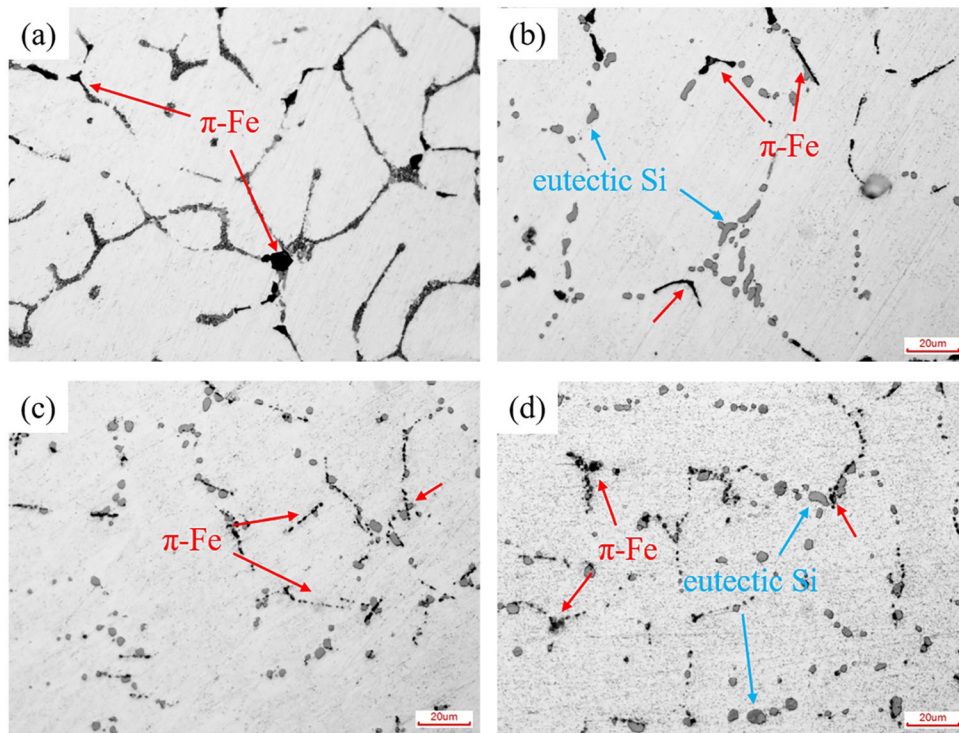


Figure 2. The OM images of the microstructure in the as-cast alloy (a) and the T6 heat-treatment alloy A (b), alloy B (c) and alloy C (d), all at 500x magnification.

Table 4. The Average Size of Eutectic Si and the Area Fraction of FIMCs in T6 Heat-Treated Alloy A, B and C

Alloy	Size of eutectic Si (μm)	Area fraction (%)		
		Needle-like π-Fe	Granular π-Fe	α-Al ₁₅ (Fe,Mn) ₂ Si ₃
A	2.11	1.86	0.13	0.19
B	1.89	0.21	1.78	0.25
C	1.95	-	0.20	2.12

For alloy B (Figure 3c, d), it was observed that the π-Fe phase particles, presenting a massive morphology in the as-cast state (Figures 1 and 2a), underwent necking and fragmented into smaller granules, indicating that the π-Fe intermetallic phases dissolved efficiently at a solution temperature of 545 °C. In alloy C (Figures 3e, f), two spherical FIMCs were detected, the larger black one was identified as α-Al₁₅(Fe, Mn)₂Si₃, and the smaller white one was recognized as π-Al₈FeMg₃Si₆(Mn). The formation of α-Al₁₅(Fe, Mn)₂Si₃ phases occurred at the expense of dissolving π-Fe phases. Additionally, a broad dispersoids free zone (DFZ) formed adjacent to the eutectic region, accompanying the precipitation of the coarse α-Al₁₅(Fe, Mn)₂Si₃ particles. Compared to π-Fe particles, the precipitation of larger α-Al₁₅(Fe, Mn)₂Si₃ particles on grain boundaries was more likely to induce crack initiation during deformation. As per the statistical analysis of the

area fraction of FIMCs, presented in Table 4, the transformation of FIMCs primarily involves the dissolution of π-Fe phases and formation of α-Al₁₅(Fe, Mn)₂Si₃ phases with an elevated solution temperature, corroborating the microstructure observation.

The EDS analyses conducted on the α-Al matrix of the as-quenched alloys A, B, and C are presented in Table 5. Post solution treatment, the concentrations of Mn and Mg in the α-Al matrix of alloys A, B, and C are recorded as 0.25, 0.23, 0.18 wt% and 0.48, 0.51, 0.40 wt%, respectively. In comparison with the element content of the as-cast matrix, it becomes apparent that the transformation of FIMCs coincides with the diffusion of Mn atoms from the matrix into the constituent particle and the Mg atoms from the π-Fe intermetallics into the matrix. Notably, this diffusion process is accelerated as the solution temperature increases.

Precipitation of Dispersoids with the Different Solution Temperatures

Figure 4 illustrates the morphology and size distribution of the dispersoids in T6 heat-treated alloys A, B, and C. The quantitative statistical outcomes concerning the mean diameter and volume fraction of these dispersoids are displayed in Table 6. Owing to the low diffusion coefficient of Mn within the α-Al matrix, the precipitation of Mn-rich dispersoids only occurs during the solution treatment, which yields sufficiently high temperatures to promote Mn

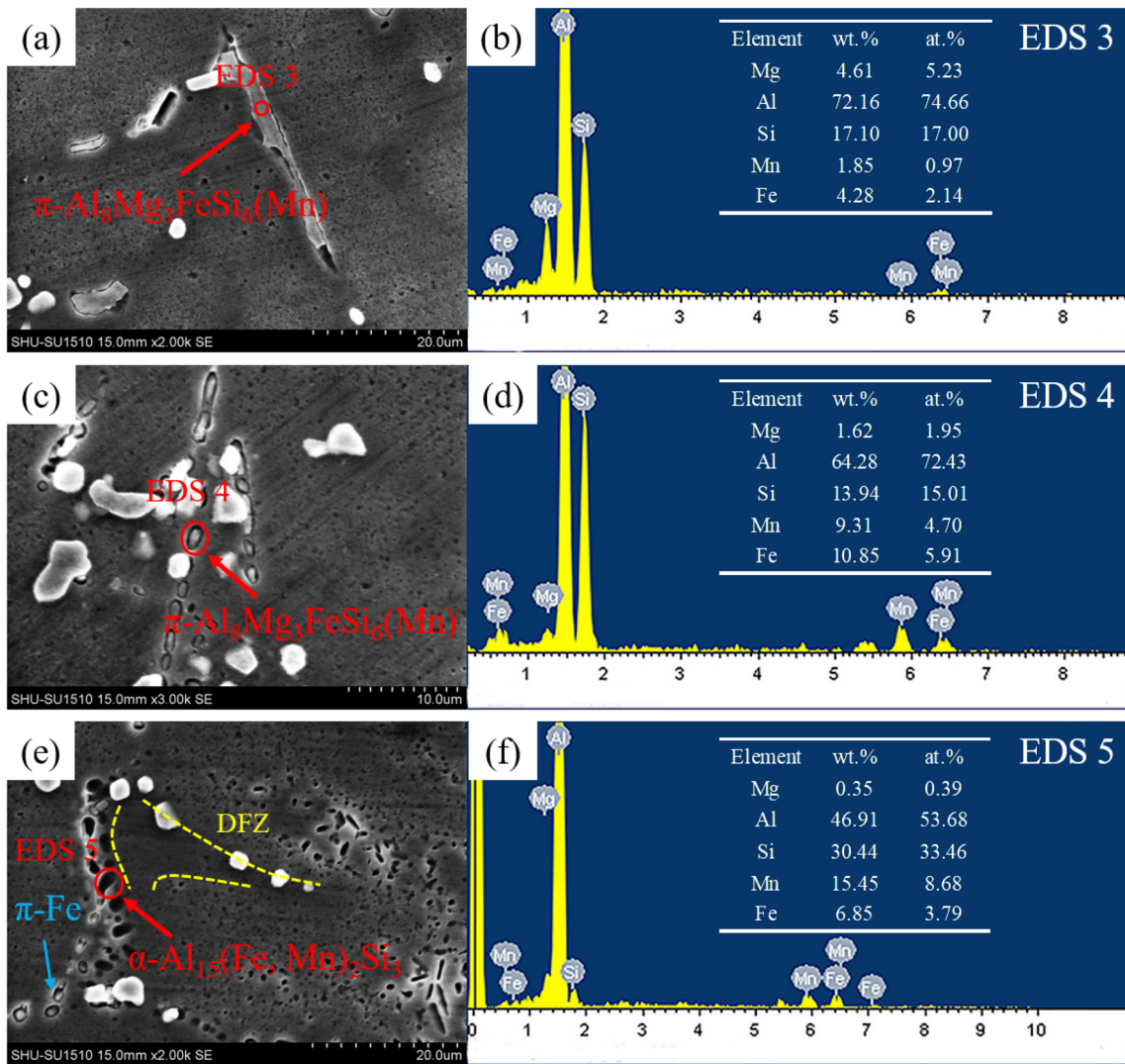


Figure 3. SEM images under high magnification and EDS analysis of the FIMCs of alloy A (a, b), alloy B (c, d) and alloy C (e, f) after the T6 heat treatment.

Table 5. The Mean Concentration of Mn, Mg and Si Elements Within the α -Al Matrix of the as-Quenched Alloy A, B and C

Alloy	Mn	Mg	Si
A	0.25±0.04	0.48±0.03	1.28±0.02
B	0.23±0.02	0.51±0.02	1.25±0.03
C	0.18±0.03	0.40±0.03	1.32±0.02

diffusion across extensive distances.¹⁴⁻¹⁶ As depicted in Figure 4a, the finest dispersoids with the least number density are formed in alloy A. With an escalated solution temperature, both the number and size of the dispersoids see an increase. In alloy B (Figure 4b), the dispersion particles showcase an almost spherical morphology, with an average diameter approximating 86 nm. When the

solution temperature further elevates to 560 °C, the dispersoids coarsen and exhibit an evident bimodal size, as observed in Figure 4c, f. This can be attributed to the fact that a higher solution temperature enlarges the growth critical size of the particles and expedites the diffusion of solute elements between particles, thus catalyzing Ostwald ripening.¹⁴

The HRTEM image and corresponding fast Fourier transform (FFT) have been utilized to analyze the crystal structure of the dispersoids, as illustrated in Figure 5a, b. The stoichiometric formula of dispersoids in all alloys, deduced from TEM-EDS analysis (Figure 5d) and FFT pattern, is $\alpha\text{-Al}_{15}(\text{Fe, Mn})_2\text{Si}_3$. The FFT in Figure 5b suggests that the $\alpha\text{-Al}(\text{Fe, Mn})\text{Si}$ phase has a BCC structure, exhibiting an orientation relationship with the $\alpha\text{-Al}$ matrix as $(1 - 1 1)_{\text{Al}} // (3 0 1)_{\alpha}$ and $[0 1 1]_{\text{Al}} // [-1 2 3]_{\alpha}$. Figure 5c showcases an inverse FFT (IFFT) of the dispersoid/matrix interface in the HRTEM image. As

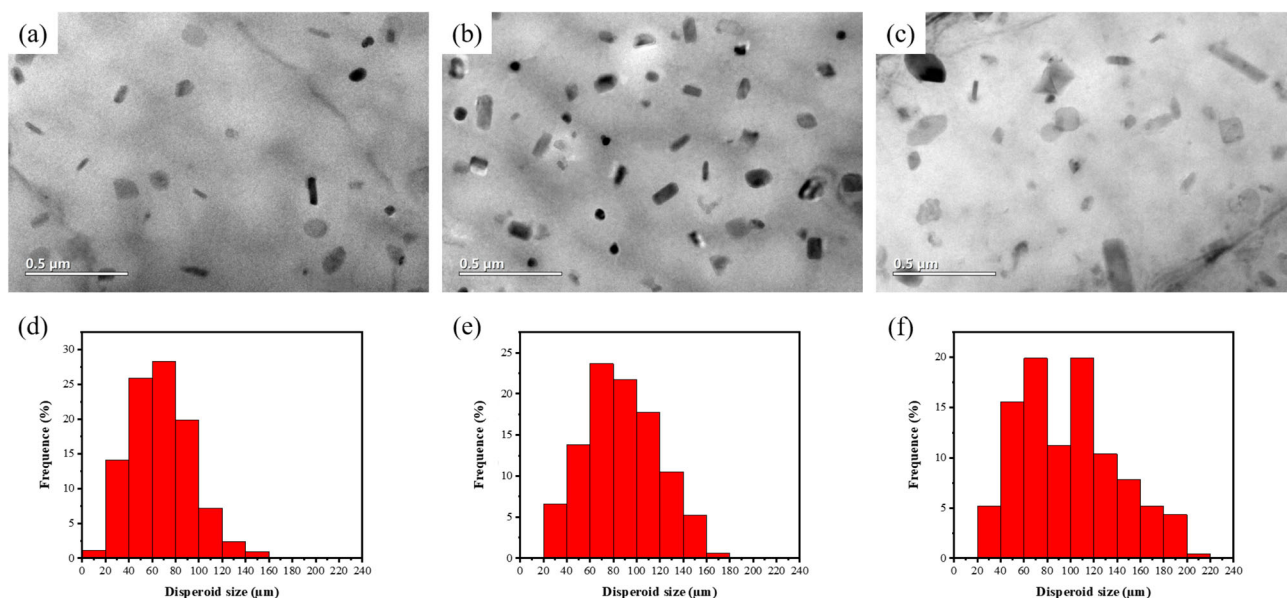


Figure 4. TEM images and the size distribution of α -AlFeMnSi dispersoids in alloy A (a, d), alloy B (b, e) and alloy C (c, f).

Table 6. The Mean Diameter and Volume Fraction of the Dispersoids in Alloy A, B and C

Alloy	Mean diameter (nm)	Volume fraction (%)
A	78	2.7
B	86	5.7
C	96	5.6

observed, the interplanar spacings of $(1 - 1 1)_{Al}$ and $(3 0 1)_{\alpha}$ are measured to be 0.237 nm and 0.205 nm, respectively. A partially coherent interface exists between the dispersoid and the matrix, with discernible dislocations. The formation of such interfacial dislocations is known to accommodate misfit between coincident planes, thus relieving interfacial stresses.

Mechanical Properties and Fracture

Figure 6 presents the mechanical properties of the as-cast alloy and T6 heat-treated alloys A, B, and C. Post T6 heat treatment, there is an enhancement in the alloy's mechanical properties, primarily in strength. Relative to the as-cast alloy, alloy A's elongation to break exhibits only a minor increment, attributable to the incomplete fragmentation of eutectic Si and poor dissolution of π -Fe phases at a solution temperature of 530 °C, as depicted in Figure 3a. Alloy B, treated at a solution temperature of 545 °C, showcases the most exceptional comprehensive mechanical properties. The yield strength (YS), ultimate tensile strength (UTS),

and elongation to fracture (E%) of T6 heat-treated alloy B are 333 MPa, 383 MPa, and 7.8%, respectively. Alloy C's strength parallels that of alloy A; however, its elongation to fracture surpasses that of alloy A, approximating that of alloy B.

Figure 7 illustrates SEM images of representative tensile-fractured surfaces of the T6 heat-treated alloys A, B, and C. With an escalating solution temperature, the alloy's fracture surfaces become rougher, as demonstrated in Figure 7a-c. A distinct river pattern is noticeable on alloy C's fractured surface. In the case of alloy A, the fracture likely consists of a mix of transgranular and intergranular types, and the propagation of damage correlates with the presence of coarse, cracked FIMCs, especially the needles, as evident in Figure 7d. Flat cleavage planes near the ruptured π -Fe phases suggest that the crack progresses directly along the sharp edge of the FIMCs to the matrix, resulting in limited ductility. The fragmentation of these needles into compact granules is only fully realized when the solution temperature exceeds 545 °C. Alloy B's fracture surface, as seen in Figure 7e, exhibits few α -Al matrix cleavages and a significant number of dimples, implying an adequately ductile fracture.⁹ Eutectic Si or FIMCs are discernible at the base of the pits. Relative to alloy B, alloy C's fracture surface displays more α -Al matrix cleavages, denoting transgranular features, and fewer, larger open pores. From Figure 7f, some eutectic Si particles and FIMCs were debonded from the matrix, while an extensive dimpled morphology unveils substantial plastic deformation in the matrix preceding fracture, restraining the initiation and propagation of cracks. Contrary to alloy A, small dimples

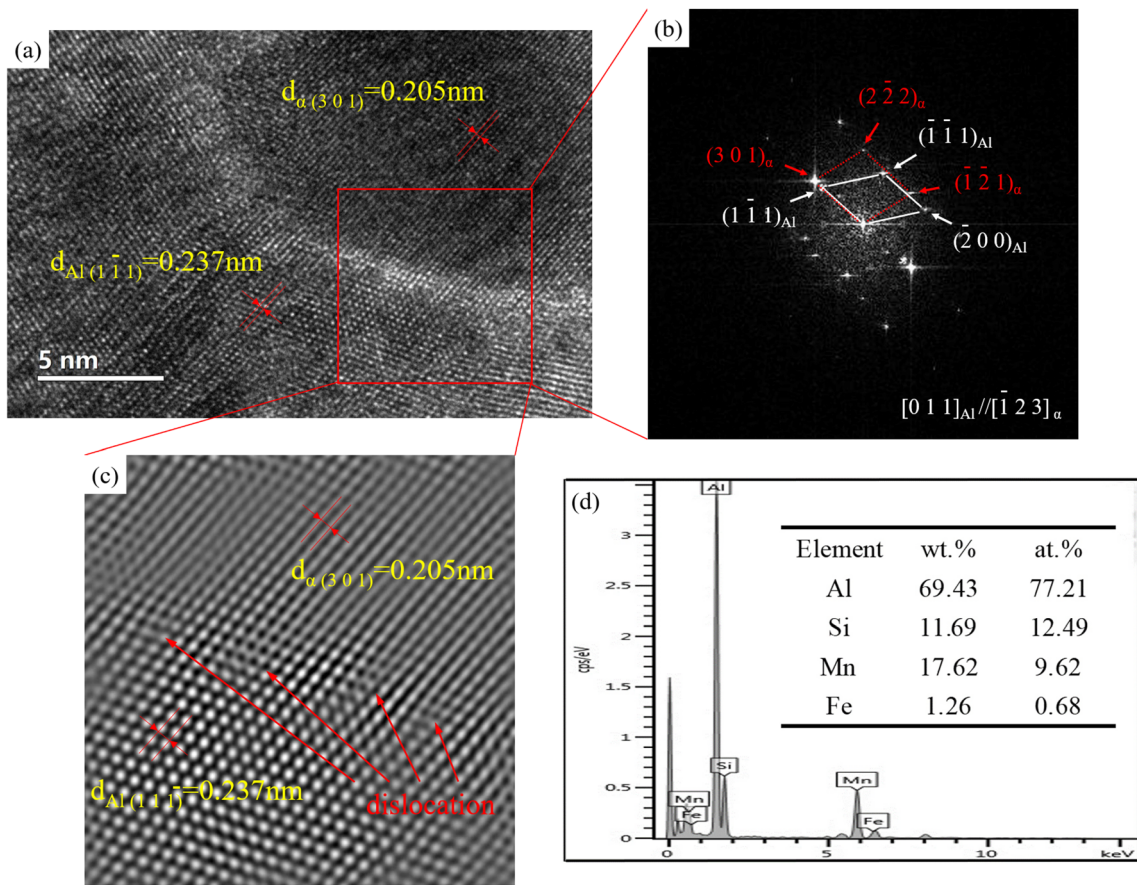


Figure 5 . (a) The HRTEM image from the α -AlFeMnSi dispersoid, (b) corresponding FFT pattern and (c) IFFT pattern and (d) EDS spectrum collected from α -AlFeMnSi dispersoid and its composition shown in the inserted table.

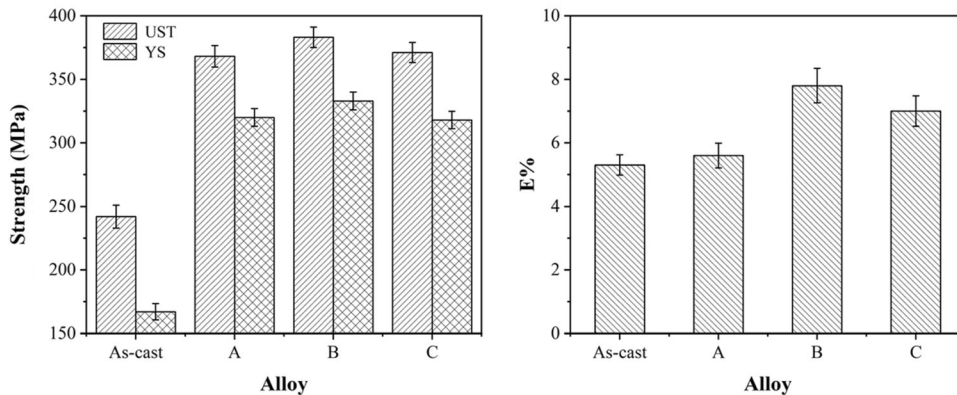


Figure 6. Mechanical properties of as-cast alloy and T6 heat-treated alloys A, B and C.

on the rough cleavage plane in alloy C indicate a tortuous crack propagation path within the matrix.

Analysis of the fracture characteristics reveals that the fracture mode transitions from a blend of transgranular and intergranular to solely intergranular and then back to a blend of transgranular and intergranular with an increase in the solution temperature from 530 to 560 °C.

Discussion

The As-Cast Microstructure

The incorporation of Mn into the Al-Si-Mg alloy exhibits a modification effect on the FIMCs. As suggested by prior studies, β -Al₅FeSi phases characterize the FIMCs in Al-Si-Mg alloys devoid of Mn, whereas the expectation for

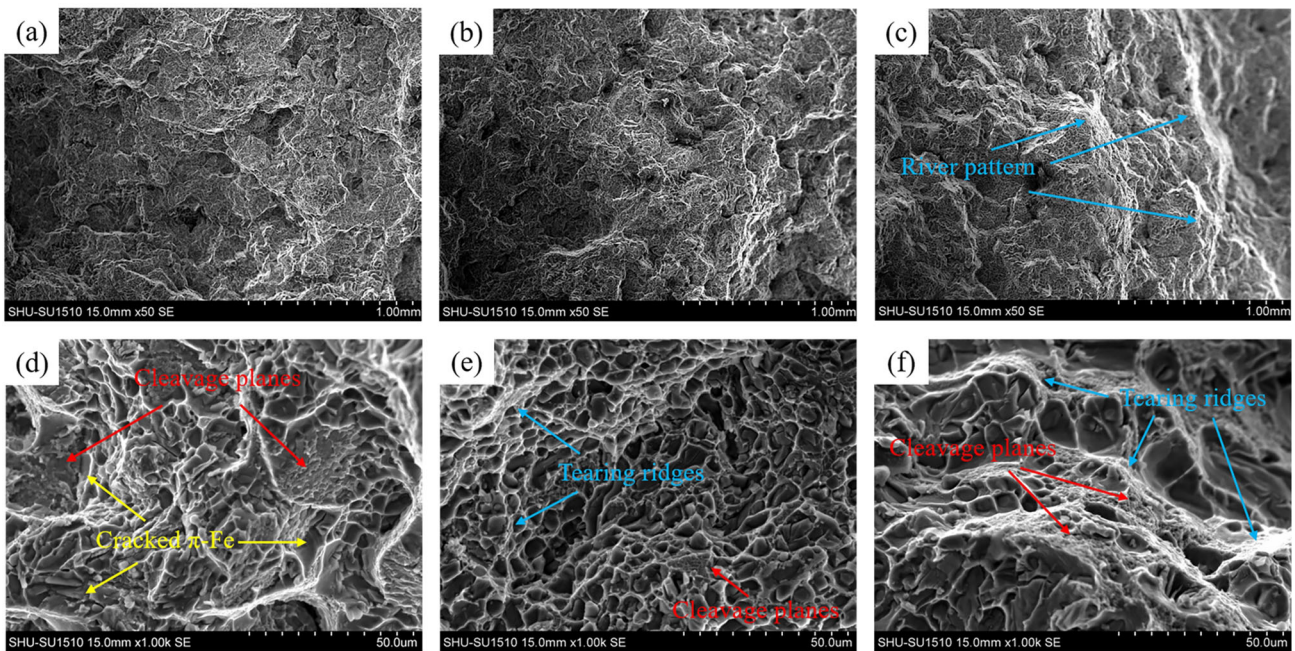


Figure 7. The fracture surfaces of T6 heat-treated alloys A (a, d), B (b, e) and C (c, f).

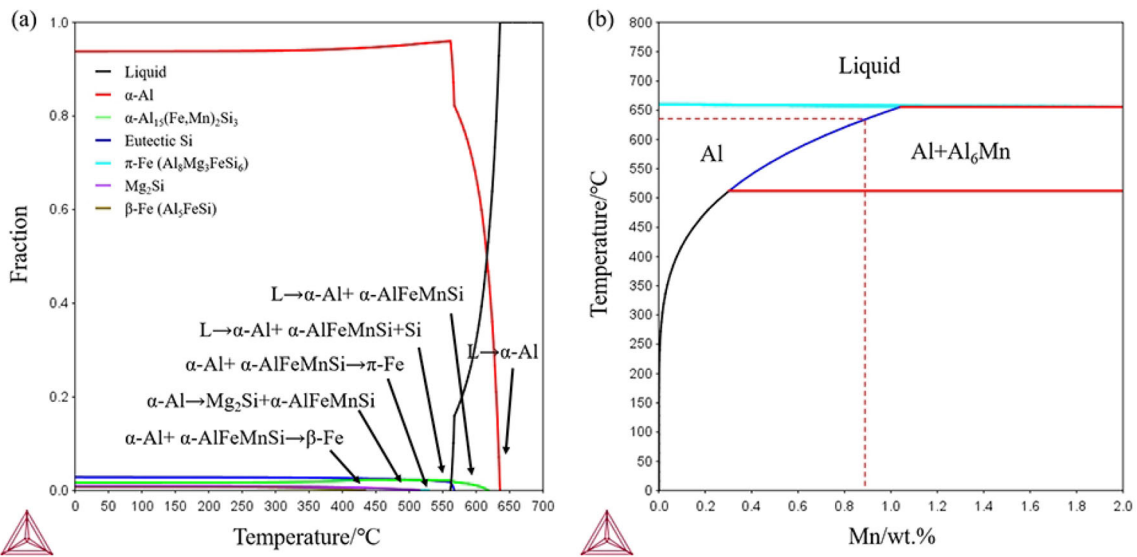


Figure 8. (a) The equilibrium solidification process of Al-3.4-0.6Mg-0.5Mn-0.2Fe alloys and phase mass fraction calculated by Thermo-Calc software and (b) Al-Mn binary phase diagram.

Al-Si-Mg alloys containing Mn is the presence of α -AlFeMnSi phases.²⁷⁻²⁹ Some Fe atoms within β -Al₃FeSi are substituted by Mn atoms, consequently transforming into α -Al₁₅(Fe, Mn)₃Si₂ with a BCC structure, which subsequently imparts a refining effect on Fe-rich particles.²⁹

The equilibrium solidification process of Al-3.4Si-0.6Mg-0.5Mn-0.2Fe alloys has been simulated using Thermo-Calc software, as illustrated in Figure 8a, indicating the predicted equilibrium primary phase as α -Al₁₅(Fe, Mn)₃Si₂. The solidification initiates with the crystallization of α -Al

phases, which is subsequently followed by the primary α -Al₁₅(Fe, Mn)₃Si₂ intermetallics. With a further decrease in temperature, the ternary eutectic reaction $L \rightarrow \alpha$ -Al + α -Al₁₅(Fe, Mn)₃Si₂ + Si takes place, and the precipitation of π -Al₈Mg₃FeSi₆(Mn) and Mg₂Si phases occurs sequentially. Nevertheless, apart from α -Al₁₅(Fe, Mn)₃Si₂ phases, coarse primary π -Al₈Mg₃FeSi₆(Mn) intermetallics are also experimentally observed, a phenomenon that can be explained by the heterogeneous precipitation of the FIMCs during non-equilibrium solidification. In the initial solidification phase, the rapid temperature decline fosters the nucleation of α -Al₁₅(Fe, Mn)₃Si₂ intermetallics due to the

high undercooling. However, Mn possesses a solid–liquid partition coefficient k of approximately 0.95 in Al as per the Al–Mn binary diagram.³⁰ According to the Scheil equation:

$$C_L = C_0 \cdot f_L^{(k-1)} \quad \text{Eqn. 1}$$

During the solidification process, the segregation concentration C_L of Mn in the interdendritic region remains notably low. The majority of Mn atoms were entrapped in the preferential crystallization of the α -Al matrix (Figure 8a) under the conditions of a high initial cooling rate. Consequently, the final as-cast microstructure exhibits Mn supersaturation (Table 3), attributable to the low diffusion coefficients of Mn in α -Al.³¹ Within the computed solidification temperature spectrum, the peak solubility of Mn in the α -Al matrix stands at 0.89% at 635 °C substantially higher than the added Mn content (0.5%) in the current research, as depicted in the Al–Mn binary phase diagram in Figure 8b. Therefore, the growth of primary α -Al₁₅(Fe, Mn)₃Si₂ intermetallics was curtailed due to the scarcity of available Mn and the constraints of solidification time.

In comparison to Mn, the solid-liquid partition coefficients of Fe and Mg in Al were approximately 0.022 and 0.5, respectively.³² During the solidification process, nearly all Fe in the alloy segregates toward the leading edge of the solid–liquid interface, facilitating the formation of FIMCs. Toward the termination of solidification, when the segregation concentration of Mn atoms in the remaining liquid phase was inadequate to fully react with Fe atoms, the surplus Fe atoms are prone to interact with Mg, which exhibited a greater segregation tendency and diffusion rate, leading to the formation of the π -Al₈Mg₃FeSi₆ phase.³³ These primary intermetallic compounds, formed directly in the liquid phase, tend to exhibit coarse morphologies and are resistant to dissolution during the solution treatment, as illustrated in Figure 1a. This characteristic may negatively impact the alloy's ductility

The emergence of non-equilibrium FIMCs in Al alloys has been extensively examined.⁹ It has been proposed that non-equilibrium solidification and heterogeneous nucleation are the principal factors contributing to the discrepancy observed between microstructural features and phase diagram calculations.³⁴ The presence of small π -Al₈Mg₃FeSi₆ intermetallics in Figure 1 can be elucidated by the peritectoid reaction α -Al + α -Al₁₅(Fe, Mn)₃Si₂ → π -Al₈Mg₃FeSi₆ occurring post-solidification, which signifies that α -Al₁₅(Fe, Mn)₃Si₂ particles may function as the heterogeneous nucleation sites for π -Al₈Mg₃FeSi₆ phases. Hence, it can be deduced that toward the end of solidification, the primary α -Al₁₅(Fe, Mn)₃Si₂ phase further facilitates the genesis of non-equilibrium primary π -Al₈Mg₃FeSi₆ phase. In this study, the rationale behind the presence of Mn atoms in the composition analysis of π -Fe intermetallics in

the as-cast alloys can likely be attributed to a composite structure where the non-equilibrium primary π -Al₈Mg₃FeSi₆ phases coexist with the primary α -Al₁₅(Fe, Mn)₃Si₂ phases. The development of π -Fe phases in aluminum alloys with high Mg content has been confirmed.^{35,36} It has been documented that the π -AlFeMgSiMn phase (Al₈Mg₃FeSi₆) typically forms on the surface of β -Al₅FeSi or α -Al₁₅(Fe, Mn)₃Si₂ phase in Al–Si–Mg–(Mn) alloys, and an increase in Mg, especially beyond 0.6%, leads to the formation of a larger number of π -AlFeMgSiMn phases with enhanced thermal stability.^{27,36} Therefore, the modification of FIMCs also hinges on high-temperature preservation during solution treatment to provide ample diffusion time for Mn and thermal activation.

The Solid-State Transformation of Fe-Rich Intermetallics and Precipitation of α -Al(Fe, Mn)Si Dispersoids at Different Solution Temperatures

SEM observations depicted in Figure 3 elucidate that the microstructural evolution of the experimental alloy during the solution treatment primarily encompasses the dissolution and transformation of π -Fe intermetallics and the precipitation of dispersoids. At various solution temperatures, the alterations in the morphology and composition of π -Fe intermetallics, in tandem with the precipitation kinetics of dispersoids, can be explicated by element diffusion and phase transition temperatures. The association among the diffusion coefficients of Mg, Mn, and Fe in the α -Al matrix can be outlined as follows^{14,33}: $D_{Mg} \gg D_{Fe} \gg D_{Mn}$.

As inferred from Section 3.1, the Mn atoms in the matrix are supersaturated under as-cast conditions. In order to maintain equilibrium composition, the diffusion of elements during solution treatment implicates two processes: (1) Dispersoids precipitate, absorbing the supersaturated solute elements in the matrix. The nucleation and growth of these dispersoids necessitate overcoming the augmented interfacial energy and elastic strain energy, demanding sufficient temperature to expedite the diffusion of elements and provide the activation energy for phase transition. (2) Surplus Mn atoms diffuse directly into pre-existing Mn-rich particles promoting their growth, a process requiring lower energy and thus more likely to transpire. The solidification process shown in Figure 8a suggests that the dissolution of π -Fe phase transpires in the temperature range (530–565 °C) between the peritectoid and eutectic reactions, and the precipitation of α -AlFeMnSi dispersoids requires close proximity to eutectic temperature (565 °C). This deviates from the typical solution temperature of traditional Al–Si alloys such as A356, which is typically 540 °C. The relationship between the diffusion of solute atoms and phase transformation at varied solution temperatures is depicted in Figure 9. With escalating solution

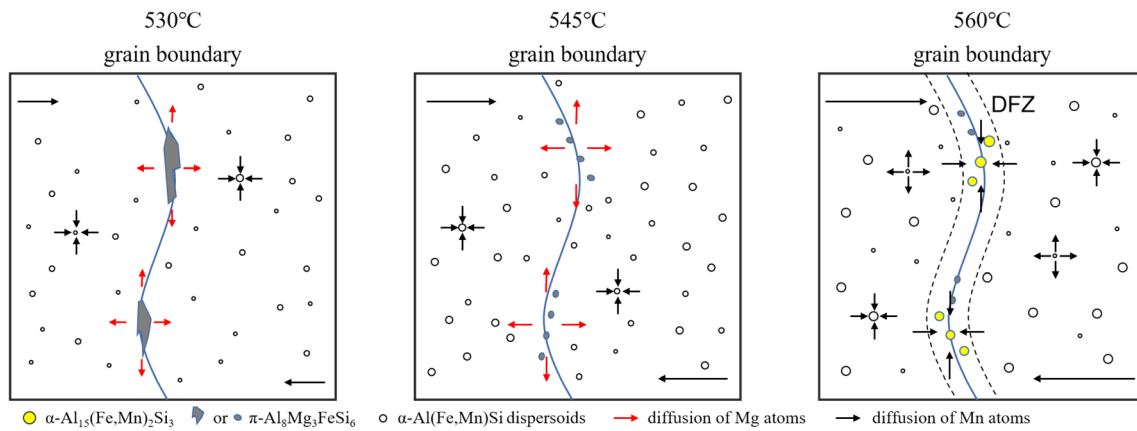


Figure 9. Schematic illustration of the diffusion of solute atoms and phase transformation at the different solution temperature.

temperature, the driving force of elemental diffusion enhances and the chemical stability of π -Fe phases is compromised, provoking the dissolution of π -Fe intermetallics and releasing Mg into the α -Al matrix. Simultaneously, the Mn element readily achieves long-range diffusion, leading to the increment of Mn content in constituent particles. Furthermore, the nucleation of dispersoids also escalates at higher temperatures due to the increased rate of elemental diffusion and thermal activation. As such, alloy B precipitated more dispersoids of comparable size relative to alloy A. Previous studies have noted that the growth kinetics of Mn-containing dispersoids is slow, attributable to the low diffusion coefficient of Mn in the Al matrix.³⁷

Upon the elevation of the solution temperature to 560 °C, the diffusion of elements notably accelerated, resulting in an increased critical size for the growth of dispersoids. Concurrently, both the dissolution and coarsening of dispersoids occur via the Ostwald ripening process, contributing to the bimodal distribution of α -AlFeMnSi dispersoids. Moreover, the low solubility of Mn and Fe elements in the matrix led to their agglomeration in the solution position of π -Fe phases. This, in turn, resulted in the formation of the α -Al₁₅(Fe, Mn)₂Si₃ phase, as depicted in Figures 3e and 9. This phase formation consumed Mn atoms around the grain boundaries, prompting the development of a broad dispersoids free zone (DFZ). However, it is crucial to note that even after the solution treatment at 560 °C for 4 h, the π -Fe intermetallics were not entirely dissolved, as shown in Figure 3e. This observation highlights the high thermal stability of π -Fe phases within the Al–Si–Mg alloy, particularly those with high Mg content.

Yield Strength

The disparate mechanical properties observed across the three T6 heat-treated alloys can be primarily ascribed to the

variation in morphology and size distribution of Fe-rich Intermetallic Compounds (FIMCs) and dispersoids. These are the primary microstructural characteristics influenced by the solution temperature. Previous studies have reported that nano-sized dispersoids interact with dislocations through the Orowan bowing mechanism, thereby contributing to the enhancement of alloy strength.¹⁵ The contribution of dispersoids to the yield strength of alloys, denoted as σ_d , can be evaluated using the Ashby–Orowan equation^{21,38}:

$$\sigma_d = \frac{0.84MGb}{2\pi(1-\nu)^{1/2}\lambda} \ln \frac{r}{b} \quad \text{Eqn. 2}$$

where M is the Taylor factor; G is shear modulus of the Al matrix; b is the Burgers vector of dislocation in Al; ν is the Poisson ratio of Al, and k is the interspacing of particles.

$$\lambda = r \left(\frac{2\pi}{3f} \right)^{1/2} \quad \text{Eqn. 3}$$

where r is the radius of particles and f is the volume fraction of particles. In accordance with Eqs. (2) and (3), the contribution of the dispersoids to yield strength is computed to be 37 MPa, 49 MPa, and 44 MPa, respectively. Upon comparing alloys A and B, the discrepancy in calculated dispersion strengthening (12 MPa) aligns closely with the difference in experimental yield strength (13 MPa). Conversely, the value of $\sigma_{dB} - \sigma_{dC}$ (5 MPa) is substantially less than the experimental yield strength difference (15 MPa) between alloys B and C. This phenomenon is attributable to the lower Mg content within the matrix of as-quenched alloy C, resulting in less precipitation of Mg–Si strengthening phases during the subsequent aging process. Numerous studies have reported that an elevated solution temperature expedites Mg diffusion into defects and oxidation, thereby attenuating the precipitation hardening effect^{39–41}. Figure 10 exhibits the DSC traces of as-quenched alloys A, B, and C to substantiate this

conclusion. Two distinct exothermic peaks on the DSC curve represent the precipitation of β'' (I) and $\beta''-\beta'$ transformation (II), respectively.^{23,42} The β'' phase is reputed to be the most potent strengthening phase in Al–Si–Mg alloys.³⁵ As can be inferred from the DSC trace, alloys A and B demonstrate similar peak I sizes, suggesting similar precipitation kinetics for β'' phases within these alloys. This similarity is due to the offsetting effects of residual Mg in the π -Fe phases and Mg oxidation caused by a temperature increase from 530 to 545 °C, thus resulting in a similar available Mg element within the matrix of as-quenched alloys A and B. Consequently, the increase in yield strength closely mirrors the difference in dispersion strengthening between alloys A and B. With the solution temperature escalating to 560 °C, a decrease in the area of peak I indicates a reduction in the volume fraction of β'' phases, which in turn diminishes the yield strength.

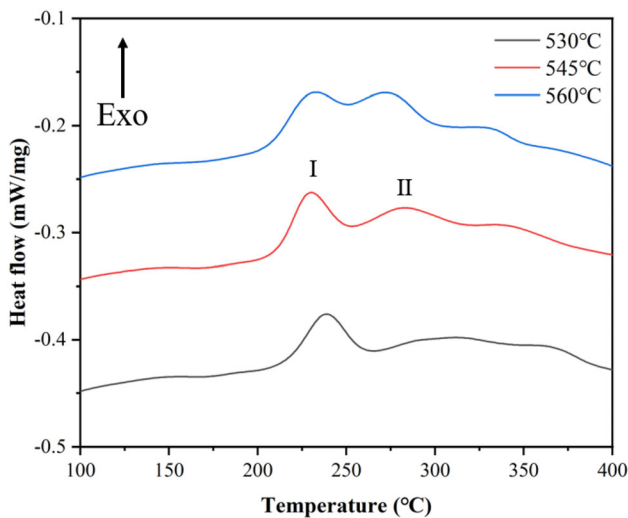


Figure 10. The heating DSC curves of the as-quenched samples solution-treated for 4h at different temperatures.

Fracture

The progression from yield to fracture in aluminum alloy encompasses three stages: plastic deformation, crack initiation, and crack propagation. As prior research on Al–Si–Mg alloys has indicated, the controlling factor for crack initiation is the attainment of a critical stress derived from the interaction between the slip band and brittle particles within the interdendritic region,^{4,33} such as eutectic Si and FIMCs. The accumulation of dislocations at coarse particles leads to a local stress build-up as the deformation progresses.⁴³ In the present study, cracking or decohesion of particles on the fracture surface of all samples was observed, as demonstrated in Figure 7. The cracking and decohesion of particles depend on the particle characteristics, with particles of larger size and aspect ratio experiencing cracking or debonding more frequently, as illustrated in Figure 11. In the case of alloy A (Figure 11a), the cracking of coarse π -Fe intermetallics served as a critical factor in the matrix cleavage. The intense local stress surrounding the hard particles increased the potential for crack initiation and resulted in inhomogeneous deformation.⁴⁴

Moreover, it has been proposed that the initiation of plastic flow triggers the growth and merging of damage events.¹⁵ For instance, the fracture of the alloy examined in this study is accompanied by the formation of a considerable number of dimples, which is generally recognized as a hallmark of ductile fracture. This indicates that significant plastic deformation transpires within the matrix prior to fracture. The distribution of plastic strain, to a certain degree, depends on the influence of non-shearable second phase particles, such as the α -AlFeMnSi dispersoids examined in this study. These particles can alter the direction of plastic flow and instigate a detour around them by pinning dislocations, as has been suggested by prior research.⁴⁵ Xu et al.⁴⁵ noted through in-situ TEM observations that moving dislocations deviated to bypass non-shearable precipitates, resulting in a zigzag route for plastic flow. Consequently, the distribution and extent of damage is influenced by the dispersal of second phase particles and the strength of the interface bond between the particle and matrix.

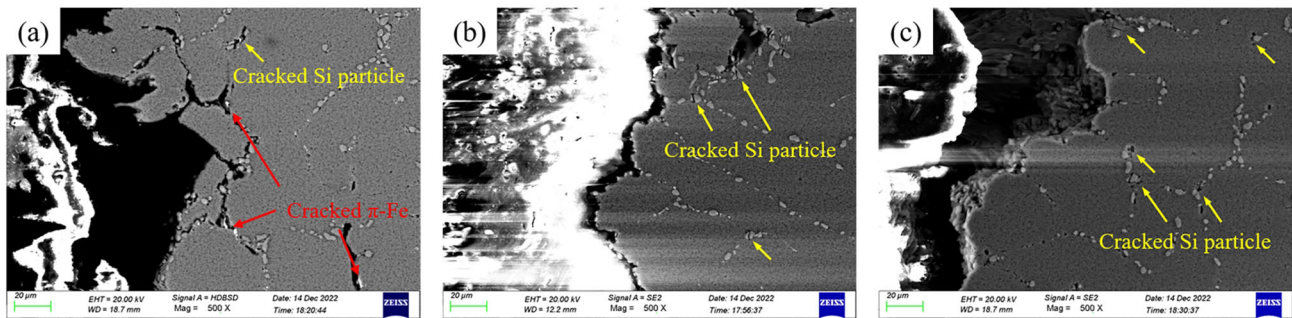


Figure 11. The SEM fractographs near the fracture surface of T6 heat-treated samples: (a) alloy A; (b) alloy B; (c) alloy C.

In the present study, for all alloys investigated, a fracture process localized at the eutectic region was discerned via the observation of Si particles and FIMCs on fracture surfaces, indicative of the coalescence of plastic flow. Observations of the cleavage characteristics on the fracture surface of alloy A suggest that cracks propagate swiftly within the matrix. This rapid propagation can be attributed to the tearing of the α -Al matrix by cracked acicular π -Fe phases featuring sharp edges, as depicted in Figure 11a. In contrast, the enhanced precipitation of fine dispersoids in alloy B can obstruct the crack propagation within the matrix. Simultaneously, void formation at the grain boundary can be impeded owing to the refinement of π -Fe phases and the presence of fine dispersoids, which effectively pin the dislocations. If dislocation is adequately pinned within the grains, stress accumulation and crack initiation at Si particles and FIMCs can be suppressed.¹³

Nevertheless, as the size of the dispersoids escalates, the damage events tend to manifest within localized shear bands in the grains, culminating in transgranular fractures, as exemplified by alloy C. Should the debonding of dispersoids and Si particles transpire concurrently, the crack could propagate by a network of micro-cracks interconnecting the dispersoids and Si particles, ultimately resulting in a mixed fracture of transgranular and intergranular types. The high elongation to fracture of alloy C can be attributed to three primary factors: (1) The robust interfacial bond between the dispersoids and the matrix fosters high critical stress for void initiation; this is evidenced by the partially coherent and clear interface between the dispersoids and the matrix, as depicted in Figure 5. (2) The dispersed distribution of dispersoids lengthens the propagation path of the microcrack, thereby impeding damage development; (3) The matrix exhibiting lower hardness possesses a higher damage tolerance limit. The oxidation of Mg at high solution temperatures contributes to an inadequate aging hardening effect. Concurrently, the DFZ can absorb dislocations to alleviate the strain proximate to grain boundaries, thereby curbing the initiation of cracks on the constituent particles.⁴⁶ Additionally, matrix softening leads to the decreased strength of alloy C. In conclusion, the failure behavior of Al–Si–Mg–Mn alloys correlates with the variations in local stress and plastic strain accumulation. Given the deformation resistance of the second phase particles to the matrix, the precipitation of fine, high-density dispersoids within the matrix can effectively equilibrate the strain accumulation disparities between grain boundaries and matrix, thereby enhancing comprehensive mechanical properties.

Conclusion

A comprehensive investigation was undertaken to elucidate the influence of solution treatment temperature (530, 545, and 560 °C) on the strength and fracture characteristics of

low-silicon cast aluminum alloy enriched with Mn. The principal conclusions are as follows:

1. The microstructure of as-cast low-silicon cast aluminum alloy, which contains Mn, comprises eutectic Si, α -Al, π -Al₈Mg₃FeSi₆(Mn), and fine α -Al₁₅(Fe, Mn)₂Si₃ intermetallics. Thermodynamic computations suggested that the anticipated equilibrium primary phase was solely α -Al₁₅(Fe, Mn)₃Si₂. The emergence of π -Al₈Mg₃FeSi₆(Mn) intermetallics in as-cast alloys was associated with non-equilibrium solidification and heterogeneous nucleation on α -Al₁₅(Fe, Mn)₂Si₃ phases.
2. During the solution treatment, the dissolution and transformation of π -Fe intermetallics were observed, which were instrumental in conferring high strength and ductility to the alloy. Additionally, the homogeneous precipitation of non-shear second phase particles within the matrix mitigated local strain accumulation during deformation. This averted the formation of voids and their subsequent growth and coalescence, thereby enhancing the overall mechanical properties.
3. An elevated solution temperature accelerated the dissolution of π -Fe intermetallics and the spheroidization of eutectic Si. A high solution temperature (560 °C) fostered the formation of α -Al₁₅(Fe, Mn)₂Si₃ intermetallics, at the expense of the dissolution of π -Fe intermetallics and dispersoids near the grain boundary. This process resulted in the establishment of a dispersoid free zone (DFZ). Conversely, at a low solution temperature (530 °C), the incomplete dissolution of π -Fe intermetallics, which sequestered a substantial quantity of Mg atoms, was not favorable to the aging hardening of the alloy.
4. The precipitation kinetics of Mn-containing dispersoids were augmented with the rise in solution temperature. The dispersion strengthening was conducive to enhancing the yield strength of the alloy. Nevertheless, an excessive solution temperature (560 °C) could incite the coarsening of dispersoids through Ostwald ripening and curtail the aging hardening effect of the alloy due to Mg oxidation.

Author Contributions Methodology, DQ and KL; Software, DQ; Validation, DQ and KL; Investigation, KL; Data Curation, DQ; Writing-Original Draft Preparation, DQ; Writing-Review and Editing, YY; Funding Acquisition, YY. All authors have read and agreed to the published version of the manuscript.

Conflict of interest The authors declare no conflict of interest relevant to this article.

REFERENCES

1. R. Chen, Y. Shi, Q. Xu, B.C. Liu, Effect of cooling rate on solidification parameters and microstructure of Al-7Si-0.3Mg-0.15Fe alloy. *Trans. Nonferrous Metals Soc. China* **24**, 1645–1652 (2014). [https://doi.org/10.1016/S1003-6326\(14\)63236-2](https://doi.org/10.1016/S1003-6326(14)63236-2)
2. M. Kaba, A. Donmez, A. Cukur et al., AlSi5Mg0.3 alloy for the manufacture of automotive wheels. *Int. Metalcast.* **12**, 614–624 (2018). <https://doi.org/10.1007/s40962-017-0191-2>
3. W.J. Gao, D.L. Qian, K. Lan et al., Investigation into the formation of inclusions in a steering knuckle casting of low-silicon cast aluminum alloy. *Int. Metalcast.* (2022). <https://doi.org/10.1007/s40962-022-00846-1>
4. M. Zhu, Z. Jian, G. Yang, Y. Zhou, Effects of T6 heat treatment on the microstructure, tensile properties, and fracture behavior of the modified A356 alloys. *Mater. Des.* **36**, 243–249 (2012). <https://doi.org/10.1016/j.matdes.2011.11.018>
5. G. Luo, X. Zhou, C. Li et al., A quantitative study on the interaction between silicon content and heat treatment on thermal conductivity of Al–Si binary alloys. *Int. Metalcast.* (2021). <https://doi.org/10.1007/s40962-021-00706-4>
6. E.A. Elsharkawi, M.H. Abdelaziz, H.W. Doty et al., Effect of β -Al₅FeSi and π -Al₈Mg₃FeSi₆ phases on the impact toughness and fractography of Al–Si–Mg-based alloys. *Int. Metalcast.* **12**, 148–163 (2018). <https://doi.org/10.1007/s40962-017-0153-8>
7. C. Puncreobutr, P.D. Lee, K.M. Kareh, T. Connolley, J.L. Fife, A.B. Phillion, Influence of Fe-rich intermetallics on solidification defects in Al–Si–Cu alloys. *Acta Mater.* **68**, 42–51 (2014). <https://doi.org/10.1016/j.actamat.2014.01.007>
8. W.W. Zhang, B. Lin, P. Cheng, D.-T. Zhang, Y.Y. Li, Effects of Mn content on microstructures and mechanical properties of Al-5.0Cu-0.5Fe alloys prepared by squeeze casting. *Trans. Nonferrous Met. Soc. China.* **23**, 1525–1531 (2013). [https://doi.org/10.1016/S1003-6326\(13\)62626-6](https://doi.org/10.1016/S1003-6326(13)62626-6)
9. S.K. Shaha, F. Czerwinski, W. Kasprzak, J. Friedman, D.L. Chen, Effect of Mn and heat treatment on improvements in static strength and low-cycle fatigue life of an Al–Si–Cu–Mg alloy. *Mater. Sci. Eng. A* **657**, 441–452 (2016). <https://doi.org/10.1016/j.msea.2016.01.015>
10. A.M.A. Mohamed, E. Samuel, A.M. Samuel et al., Effect of intermetallics and tramp elements on porosity formation and hardness of Al–Si–Mg and Al–Si–Cu–Mg Alloys. *Int. Metalcast.* **17**, 664–681 (2023). <https://doi.org/10.1007/s40962-022-00813-w>
11. Z.P. Que, Y. Wang, Z. Fan, Formation of the Fe-containing intermetallic compounds during solidification of Al–5Mg–2Si–0.7Mn–1.1Fe alloy. *Metall. Mater. Trans.* **49**, 2173–2181 (2018). <https://doi.org/10.1007/s11661-018-4591-6>
12. T.A. Costa, M. Dias, L.G. Gomes, O.L. Rocha, A. Garcia, Effect of solution time in T6 heat treatment on microstructure and hardness of a directionally solidified Al–Si–Cu alloy. *J. Alloys Compd.* **683**, 485–494 (2016). <https://doi.org/10.1016/j.jallcom.2016.05.099>
13. A.R. Farkoosh, X. Grant-Chen, M. Pekguleryuz, Dispersoid strengthening of a high temperature Al–Si–Cu–Mg alloy via Mo addition. *Mater. Sci. Eng. A* **620**, 181–189 (2015). <https://doi.org/10.1016/j.msea.2014.10.004>
14. A.R. Farkoosh, X.G. Chen, M. Pekguleryuz, Interaction between molybdenum and manganese to form effective dispersoids in an Al–Si–Cu–Mg alloy and their influence on creep resistance. *Mater. Sci. Eng. A* **627**, 127–138 (2015). <https://doi.org/10.1016/j.msea.2014.12.115>
15. W.J. Poole, X. Wang, J.D. Embury, D.J. Lloyd, The effect of manganese on the microstructure and tensile response of an Al–Mg–Si alloy. *Mater. Sci. Eng. A* **755**, 307–317 (2019). <https://doi.org/10.1016/j.msea.2019.03.015>
16. C.L. Liu, Q. Du, N.C. Parson, W.J. Poole, The interaction between Mn and Fe on the precipitation of Mn/Fe dispersoids in Al–Mg–Si–Mn–Fe alloys. *Scrip. Mater.* **152**, 59–63 (2018). <https://doi.org/10.1016/j.scriptamat.2018.04.012>
17. Y.J. Li, L. Arnberg, Quantitative study on the precipitation behavior of dispersoids in DC-cast AA3003 alloy during heating and homogenization. *Acta Mater.* **51**, 3415–3428 (2003). [https://doi.org/10.1016/S1359-6454\(03\)00160-5](https://doi.org/10.1016/S1359-6454(03)00160-5)
18. R. Hu, T. Ogura, H. Tezuka, T. Sato, Q. Liu, Dispersoid formation and recrystallization behavior in an Al–Mg–Si–Mn alloy. *J. Mater. Sci. Technol.* **26**, 237–243 (2010). [https://doi.org/10.1016/S1005-0302\(10\)60040-0](https://doi.org/10.1016/S1005-0302(10)60040-0)
19. A.M.F. Muggerud, E.A. Mørtsell, Y. Li, R. Holmestad, Dispersoid strengthening in AA3xxx alloys with varying Mn and Si content during annealing at low temperatures. *Mater. Sci. Eng. A* **567**, 21–28 (2013). <https://doi.org/10.1016/j.msea.2013.01.004>
20. Q. Du, W.J. Poole, M.A. Wells, N.C. Parson, Microstructure evolution during homogenization of Al–Mn–Fe–Si alloys: modeling and experimental results. *Acta Mater.* **61**, 4961–4973 (2013). <https://doi.org/10.1016/j.actamat.2013.04.050>
21. Y.J. Li, A.M.F. Muggerud, A. Olsen, T. Furu, Precipitation of partially coherent α -Al(Mn, Fe)Si dispersoids and their strengthening effect in AA 3003 alloy. *Acta Mater.* **60**, 1004–1014 (2012). <https://doi.org/10.1016/j.actamat.2011.11.003>
22. E. Sjölander, S. Seifeddine, The heat treatment of Al–Si–Cu–Mg casting alloys. *J. Mater. Proc. Technol.* **210**, 1249–1259 (2010). <https://doi.org/10.1016/j.jmatprotec.2010.03.020>
23. R. Chen, Q.Y. Xu, H.T. Guo, Z.Y. Xia, Q.F. Wu, B.C. Liu, Correlation of solidification microstructure

- refining scale, Mg composition and heat treatment conditions with mechanical properties in Al-7Si-Mg cast aluminum alloys. *Mater. Sci. Eng. A* **685**, 391–402 (2017). <https://doi.org/10.1016/j.msea.2016.12.051>
24. I. Alfonso, C. Maldonado, G. Gonzalez, A. Bedolla, Effect of Mg content and solution treatment on the microstructure of Al-Si-Cu-Mg alloys. *J. Mater. Sci.* **41**, 1945–1952 (2006). <https://doi.org/10.1007/s10853-006-4494-y>
 25. H. Yang, S. Ji, W. Yang, Y. Wang, Z. Fan, Effect of Mg level on the microstructure and mechanical properties of die-cast Al-Si-Cu alloys. *Mater. Sci. Eng. A* **642**, 340–350 (2015). <https://doi.org/10.1016/j.msea.2015.07.008>
 26. X.Y. Wu, H.R. Zhang, F.X. Zhang, Z. Ma, L.N. Jia, B. Yang, T.T.X. Tao, H. Zhang, Effect of cooling rate and Co content on the formation of Fe-rich intermetallics in hypoeutectic Al7Si0.3Mg alloy with 05%Fe. *Mater. Char.* **139**, 116–124 (2018). <https://doi.org/10.1016/j.matchar.2018.02.029>
 27. D.L. Qian, T.F. Cheng, W.J. Gao, Y.T. Yang, Microstructure evolution and mechanical properties of low-silicon cast aluminium alloys with varying Mn contents. *Philos. Mag.* **101**, 1511–1525 (2020). <https://doi.org/10.1080/14786435.2021.1912846>
 28. S. Ji, W. Yang, F. Gao, D. Watson, Z. Fan, Effect of iron on the microstructure and mechanical property of Al-Mg-Si-Mn and Al-Mg-Si diecast alloys. *Mater. Sci. Eng. A* **564**, 130–139 (2013). <https://doi.org/10.1016/j.msea.2012.11.095>
 29. S. Belmares-Perales, M. Castro-Roman, M. Herrera-Trejo, L.E. Ramirez-Vidaurre, Effect of cooling rate and Fe/Mn weight ratio on volume fraction of α -AlFeSi and β -AlFeSi phases in Al-7.3Si-3.5Cu alloy. *Metals Mater. Int.* **14**, 307–314 (2008). <https://doi.org/10.3365/met.mat.2008.06.307>
 30. L.F. Mondolfo, *Aluminium Alloys: Structure and Properties* (UK, London, 1976), p.324
 31. Y. Du, Y.A. Chang, B.Y. Huang, W.P. Gong, Z.P. Jin, H.H. Xu, Z.H. Yuan, Y. Liu, Y.H. He, F.Y. Xie, Diffusion coefficients of some solutes in fcc and liquid Al: critical evaluation and correlation. *Mater. Sci. Eng. A* **363**, 140–151 (2003). [https://doi.org/10.1016/S0921-5093\(03\)00624-5](https://doi.org/10.1016/S0921-5093(03)00624-5)
 32. O. Pracha, O. Trudonoshynb, P. Randelzhoferb, C. Körnerb, K. Dursta, Effect of Zr, Cr and Sc on the Al-Mg-Si-Mn high-pressure die casting alloys. *Mater. Sci. Eng. A* **759**, 603–612 (2019). <https://doi.org/10.1016/j.msea.2019.05.038>
 33. B.R. Zhang, L.K. Zhang, Z.M. Wang, A.J. Gao, Achievement of high strength and ductility in Al-Si-Cu-Mg alloys by intermediate phase optimization in as-cast and heat treatment conditions. *Materials* **13**, 647 (2020). <https://doi.org/10.3390/ma13030647>
 34. Z.P. Que, C.L. Mendis, Heterogeneous nucleation and phase transformation of Fe-rich intermetallic compounds in Al-Mg-Si alloys. *J. Alloys. Compd.* **836**, 155515 (2020). <https://doi.org/10.1016/j.jallcom.2020.155515>
 35. X.Y. Wu, H.R. Zhang, Z. Ma, T.X. Tao, J. Gui, W. Song, B. Yang, H. Zhang, Interactions between Fe-rich intermetallics and Mg-Si phase in Al-7Si-xMg alloys. *J. Alloys. Compd.* **786**, 205–214 (2019). <https://doi.org/10.1016/j.jallcom.2019.01.352>
 36. Q.G. Wang, Microstructural effects on the tensile and fracture behavior of aluminum casting alloys A356/357. *Metall. Mater. Trans.* **34**, 2887–2899 (2003). <https://doi.org/10.1007/s11661-003-0189-7>
 37. C.J. Kuehmann, P.W. Voorhees, Ostwald ripening in ternary alloys. *Metall. Mater. Trans. A* **27**, 937–943 (1996). <https://doi.org/10.1007/BF02649761>
 38. A.J. Ardell, Precipitation hardening. *Metall. Trans. A* **16**, 2131–2165 (1985). <https://doi.org/10.1007/BF02670416>
 39. R. Chen, Q.Y. Xu, Z.N. Jia, B.C. Liu, Precipitation behavior and hardening effects of Si-containing dispersoids in Al-7Si-Mg alloy during solution treatment. *Mater. Des.* **90**, 1059–1068 (2016). <https://doi.org/10.1016/j.matdes.2015.11.069>
 40. H.J. Kang, H.S. Jang, S.H. Oh, P.H. Yoon, G.H. Lee, J.Y. Park, E.S. Kim, Y.S. Choi, Effects of solution treatment temperature and time on the porosities and mechanical properties of vacuum die-casted and T6 heat-treated Al-Si-Mg alloy. *Vacuum* **193**, 110536 (2021). <https://doi.org/10.1016/j.vacuum.2021.110536>
 41. H.C. Long, J.H. Chen, C.H. Liu, D.Z. Li, Y.Y. Li, The negative effect of solution treatment on the age hardening of A356 alloy. *Mater. Sci. Eng. A* **566**, 112–118 (2013). <https://doi.org/10.1016/j.msea.2012.12.093>
 42. Y. Birol, Response to artificial ageing of dendritic and globular Al-7Si-Mg alloys. *J. Alloys Compd.* **484**, 164–167 (2009). <https://doi.org/10.1016/j.jallcom.2009.05.043>
 43. Q. Cai, C.L. Mendis, I.T.H. Chang, Z.Y. Fan, Microstructure evolution and mechanical properties of new die-cast AlSi-Mg-Mn alloys. *Mater. Des.* **187**, 108394 (2020). <https://doi.org/10.1016/j.matdes.2019.108394>
 44. D.F. Mo, G.Q. He, Z.F. Hu, X.S. Liu, W.H. Zhang, Effect of microstructural features on fatigue behavior in A319-T6 aluminum alloy. *Mater. Sci. Eng. A* **527**, 3420–3426 (2010). <https://doi.org/10.1016/j.msea.2010.02.055>

45. M.N. Xu, N. Li, X.C. Sha, Y. Liu, B. Gao, L.R. Xiao, X.F. Chen, H. Zhou, In-situ TEM observations on interaction of basal $\langle a \rangle$ dislocations and β' phases in a Mg-Gd binary alloy. *Mater. Sci. Eng. A* **841**, 143017 (2022). <https://doi.org/10.1016/j.msea.2022.143017>
46. R.M. Su, Y.D. Qu, X. Li, J.H. You, R.D. Li, Effect of retrogression and reaging on stress corrosion cracking of spray formed Al alloy. *Mater. Sci. Appl.* **7**, 1–7 (2016). <https://doi.org/10.4236/msa.2016.71001>

Publisher's Note Springer Nature remains neutral with regard to jurisdictional claims in published maps and institutional affiliations.

Springer Nature or its licensor (e.g. a society or other partner) holds exclusive rights to this article under a publishing agreement with the author(s) or other rightsholder(s); author self-archiving of the accepted manuscript version of this article is solely governed by the terms of such publishing agreement and applicable law.